Degradation of Atrazine over a heterogeneous photo-fenton process with iron modified MCM-41 materials

Tamara B. Benzaquén[a], Natalia I. Cuello[a], Orlando M. Alfano[b], Griselda A. Eimer[a],[*]

[a] CITeQ (UTN-CONICET) Maestro López y Cruz Roja Argentina, Ciudad Universitaria, 5016 Córdoba, Argentina
[b] INTEC (UNL-CONICET) Ruta Nacional N°168, 3000 Santa Fe, Argentina

ARTICLE INFO

ABSTRACT

In this work, MCM-41 materials have been synthesized and modified with different metal loadings of iron by the wet impregnation method. The different meso-structures obtained were characterized by XRD, UVVIS-RD, ICP and TEM and their behaviors as heterogeneous catalysts in the photo-Fenton reaction were studied. Thus, iron-containing mesostructured materials have been successfully tested for the heterogeneous photo-Fenton degradation of atrazine aqueous solutions using UV–vis irradiation at room temperature and close to neutral pH. In order to assess the effectiveness of the herbicide degradation in the heterogeneous photo-Fenton process, and to compare experimental results obtained, a study of the photonic efficiency is presented. The photonic efficiency of Atrazine degradation was evaluated considering different experimental conditions employed two factorial designs. The results showed that the iron modified MCM-41 with a nominal metal loading of 2.5 wt.% exhibited the highest activity. Consequently, the high performance of this material indicates that the heterogeneous via of the photo-Fenton process can also be efficiently employed for the treatment of simulated wastewater containing atrazine, thus presenting advantages unlike the homogeneous process.

1. Introduction

Nowadays, the use of agrochemicals is one of the most important factors that have brought about the current yield productivity. Due to this, the market has grown quickly during the past years and its continuous increase is forecasted for the next years. Fortunately, awareness has been growing when considering the possible effects that herbicides and their degradation products may have on humans and aquatic ecosystems.

Although wastewater treatment with conventional biological processes are often the most cost-effective alternative of all treatment options, different industrial wastewaters containing toxic or biorecalcitrant organic pollutants cannot be treated with these processes [1,2]. In recent years, to overcome this drawback, the applications of Advanced Oxidation Processes (AOP's) have emerged as an important alternative for the efficient removal of organic pollutants [3]. These destruction techniques are based on the generation of hydroxyl radicals (·OH), which possess high reactivity and low selectivity. Particularly, the oxidation system based on the Fenton's reagent, hydrogen peroxide (H_2O_2) in the presence of iron species, has been used as a powerful source of oxidative radicals. More recently, the Fenton process has been shown to be enhanced by UV-light [3]. Therefore, these processes

appear as effective alternative methods to treat recalcitrant organic pollutants (like most agrochemicals) [1,2] because they may produce the rupture of these organics into smaller, less toxic and more biodegradable fragments, thereby enabling a subsequent biological treatment.

Nevertheless, it has been reported that Fenton and photo-Fenton homogeneously catalyzed reactions sometimes require high concentrations of iron in solution. Therefore, in order to remove the iron ions from solution, precipitation and re-dissolution techniques are necessary with the additional operational costs. Moreover, under near-neutral pH conditions a low efficiency of such systems is observed. This reduced efficiency is mainly due to the generation of insoluble forms of Fe^{3+} under neutral pH conditions which produce very low yield of ·OH in the presence of H_2O_2. These reasons have promoted the development of heterogeneous photo-Fenton processes based on heterogeneous catalytic systems, which provide an easy separation and recovery of the catalyst from the treated wastewater. Therefore, unlike homogeneous photo-Fenton reaction, immobilized Fenton catalytic systems provide the possibility of working in a wider pH range.

The critical point of these heterogeneous systems is associated to the resistance of immobilized metal species to be leached out into the solution. Thus, one of the aims in this research field is to prepare stable

* Corresponding author.
   E-mail address: geimer@frc.utn.edu.ar (G.A. Eimer).

materials that require the lowest oxidant to catalyst ratio for obtaining good degradation rates.

In specific literature, different organic and inorganic materials have been already reported as supports for the immobilization of active iron species in heterogeneous photo-Fenton processes [4,5]. Banić et al. [6] have recently reported the photo-degradation of an insecticide using Fe/TiO$_2$ as a heterogeneous photo-Fenton catalyst. On the other hand, Du et al. [7] have investigated the atrazine oxidation using Tantalum (oxy)nitrides for the photo-Fenton-like degradation. Many studies have shown that mesoporous structures are preferred for agrochemicals degradation [8]. Thus, the application field of these materials has been extended to environmental technology. In this sense, MCM-41 [9] is one of the most attractive porous materials because of its characteristic well-ordered structure with a hexagonal arrangement, thermal stability, large specific area ($> 1000 \, m^2 \, g^{-1}$), large pore volume ($\approx 1.3 \, mL \, g^{-1}$) and uniform mesopores with controllable diameter of 2–10 nm [10]. In addition, it can be expected that different synthetic methods result in different environments of the active sites introduced to MCM-41, which may behave differently in catalytic reactions [11,12]. Although the most extensively studied method for the introduction of active sites is the direct hydrothermal method, this tends to incorporate metal ions inside the framework of MCM-41. Then, the wet impregnation method can be able to provide metal species dispersed on the mesopores wall surface of MCM-41, giving place to catalytically active sites more accessible to reagents.

In the present work, mesoporous molecular sieves (MCM-41) were synthesized by wet impregnation with different iron loadings for their utilization in the degradation of a model pollutant (atrazine, ATZ) by heterogeneous photo-Fenton process. For this, a multivariate analysis has been used to assess the initial reaction conditions that give the best result in terms of organic degradation and catalyst stability.

2. Materials and methods

2.1. Synthesis of the catalysts

The mesoporous molecular sieves, MCM-41, were synthesized under basic pH conditions, as previously reported by Elías et al. [13]. Thus CTA (C$_{19}$H$_{42}$BrN, cetyltrimethylammonium bromide) was used as template and TEOS (Si(OC$_2$H$_5$)$_4$, tetraethoxysilane) as silicon source. The obtained solid was filtered off, washed with distilled water, and dried at 60 °C overnight. Then, the template was removed under N$_2$ flow to 500 °C and subsequently calcined at 500 °C under air flow. This solid was modified with iron by the wet impregnation method. Different concentrations of an aqueous solution of the metal precursor, (Fe(NO$_3$)$_3$·9H$_2$O), were used to reach the desired metal loadings (1, 2.5, 5, 10 and 15 wt.%). Finally, the resulting solid was dried in oven at 60 °C for 12 h and calcined at 500 °C for 9 h. The materials were designated as Fe/MCM-41(x), where x indicates the nominal metal loading in wt.%.

2.2. Chemicals

Atrazine (2-chloro-4-(ethylamino)-6-(isopropylamino)-s-triazine, C$_8$H$_{14}$ClN$_5$) chromatographic quality ($\geq$98%, Sigma-Aldrich) as a standard for calibration and commercial formulation ($\geq$90%, SYNGENTA) were chosen as the reference compounds. Ferric salt (for homogeneous photo-Fenton reactions) (Fe(SO$_4$)$_3$·8.87H$_2$O, Carlo Erba, RPE) and hydrogen peroxide (H$_2$O$_2$, 30% w/v solution, Ciccarelli p.a) were used as photo-Fenton reagents.

2.3. Device and procedures

Photo-Fenton tests were carried out in an isothermal, batch reactor (Fig. 1). The reactor (V$_R$ = 85 cm^3) was made of borosilicate glass tube with four tubular UV–vis lamps (ACTINIC BL 20, Philips, 350–400 nm

range with two bands at 404 and 438 nm). The reactor included a sintered glass piece placed at the bottom through which an air flow was introduced to provide good mixing conditions. Also, the experimental setup had an all-glass heat exchanger connected to a thermostatic bath, to keep the temperature constant during the reaction. Moreover, the reactor was equipped with a liquid sampling valve and temperature and pH controls.

The suspended catalyst in ATZ aqueous solution was mixed through the annular space. The initial concentration of the herbicide was 30 mg L^{-1}, which is the value expected in wastewater to be treated. The suspension volume employed in all of the experiments was 0.5 L.

A set of experimental runs for homogeneous and heterogeneous photo-Fenton reactions was performed, using different values of the iron initial concentration (C$^0_{Fe/MCM-41(X)}$ or C$^0_{CAT}$), the H$_2$O$_2$ to the ATZ initial molar ratio (R = C$^0_{H2O2}$/C$^0_{ATZ}$) and radiation levels. As known, these parameters have important effects on the photo-Fenton process in the homogeneous and heterogeneous phase. Furthermore, optimum values of these parameters frequently depend on the pollutant compound.

2.3.1. Homogeneous photo-Fenton reactions

An experimental run began when the previously prepared ATZ and ferric sulphate solutions were incorporated in the reactor with distilled water, and the pH was adjusted to 2.8–3 with concentrated sulfuric acid. Afterwards, the required amount of H$_2$O$_2$ solution was added and the first sample was withdrawn; this operation defined the starting time of the reaction. Prior to analysis, the thermal reaction was suddenly quenched by adding methanol to the sample. Experimental runs were performed at constant temperature (25 °C) during 120 min, and liquid samples were taken at equal time intervals (30 min). Once the run was completed, the total system was washed employing distilled water.

2.3.2. Heterogeneous photo-Fenton reactions

In this case, experimental runs began when the suspended catalyst in ATZ aqueous solution was stirred in the dark, under air flow, for 60 min in order to reach the adsorption/desorption equilibrium. After this adsorption period, the required amount of H$_2$O$_2$ solution was added, the ATZ aqueous solution was incorporated in the reactor and the first sample was withdrawn (reaction time equal to zero) to start the irradiated experiment. Runs lasted 240 or 300 min, and liquid samples were taken at equal time intervals and filtered. The measured pH of the suspension was around 5–5.5 and it has been experimentally verified that this value remains almost constant throughout the run.

2.4. Analytical methods

Aliquots of the aqueous suspensions were collected to perform the following determinations:

(i) ATZ concentration by HPLC (Perkin Elmer, Series 200), using reverse phase liquid chromatography equipped with a UV detector and a C18 column. The eluent was a binary mixture of distilled water and methanol (proportion 40:60); the eluent flow rate was 1 mL min^{-1} and the detection was performed at 221 nm.

(ii) H$_2$O$_2$ by means of a modified iodimetric technique using a UV-VIS Jasco V-650 spectrometer, at 350 nm [14].

(iii) Ferrous ions and total iron (for homogeneous photo-Fenton reaction) were measured with a standard spectrophotometric technique (Fe^{2+}-phenanthroline complex, at 510 nm) [15]. Samples for total iron determination were first treated with ascorbic acid.

2.5. Characterization

X-ray diffraction patterns (XRD) were obtained using a Philips PW 3830 diffractometer with Cu-Kα radiation (λ = 1.5418 Å). Diffraction data were recorded in the 2 h range of 1.5–7° at an interval of 0.01° and
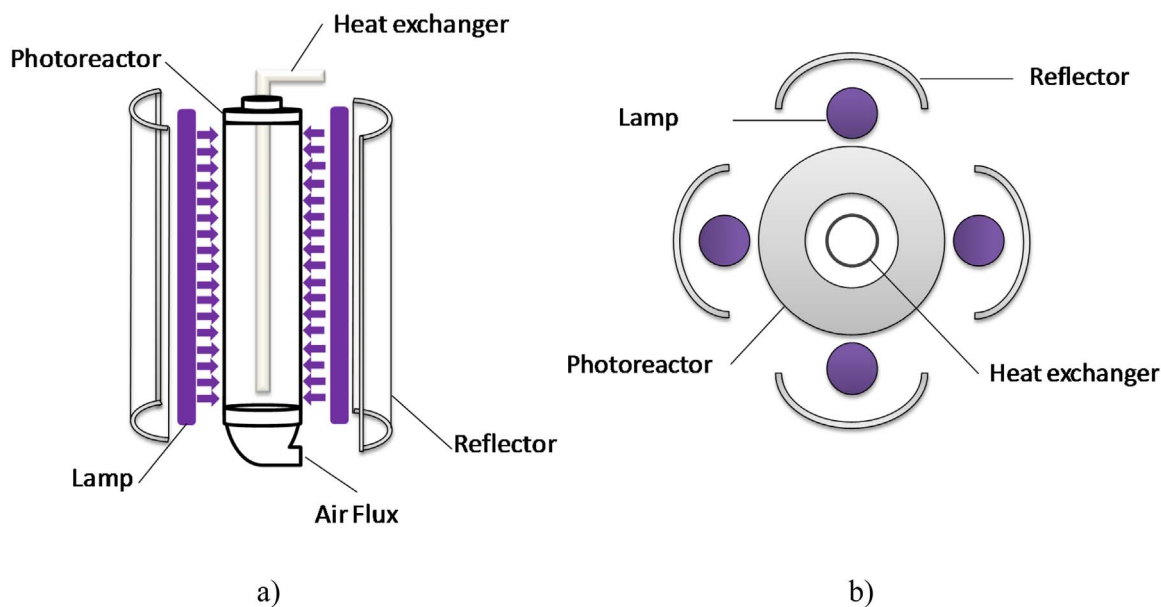
Fig. 1. Schematic representation of the photoreactor a) Side view and b) Top view.

a scanning speed of 0.6° min^{-1} and 20–80° at an interval of 0.04° and a scanning speed of 0.5° min^{-1}. The specific surface, the pore size distribution and the total pore volume were determined from N$_2$ adsorption–desorption isotherms obtained at $-196\,°C$ using a Micromeritics ASAP 2010. The surface was determined by the Brunauer–Emmett–Teller (BET) method in the pressure range of P/P$_0$: 0.01–0.21. Pore size distribution curves were determined by the NLDFT method [16]. Transmission electron microscopy (TEM) observations and selected area diffraction patterns were performed in a Philips CM200UT microscope. Samples were prepared by dispersing a small amount of powder in ethanol and depositing a drop of this emulsion on a holey carbon-coated copper grid.

Furthermore, materials were characterized by UV–vis diffuse reflectance (UV–vis DR). The spectra in absorbance mode were recorded using a Jasco V 650 spectrometer with an integrating sphere, in the wavelength range of 200–900 nm. The original spectra obtained were fitted by three Gaussian–Lorenz bands using the conventional least squares method. Curve-fitting calculations were useful in determining each band location and relative area, with confidence levels given by $R^2 \geq 0.99$.

The iron content was determined by ICP (inductively coupled plasma optical emission spectroscopy) using a VISTA-MPX CCD Simultaneous ICP-OESVARIAN. XPS analyses were performed on a computer equipped with a Multi-technique Specs Dual X-ray source Mg/Al model XR50 and a hemispherical analyzer: 150 PHOIBOS Fixed transmission mode analyzer (FAT).

3. Photonic efficiency

A parameter that is very useful when comparing different photocatalysts is the photonic efficiency (ξ). It is defined by Braslavsky et al. [17] and Benzaquén et al. [18] as "the ratio of the number of reactant molecules degraded during a given time interval, to the total number of photons arrived at the reactor wall, during the same period of time". Then, the photonic efficiency of ATZ degradation (ξ_{ATZ}), can be expressed as follows:

$$\xi_{ATZ} = \frac{\{reaction\ rate\ of\ Atrazine\}}{\{rate\ of\ photon\ arriving\ at\ the\ reactor\ wall\}} \quad (1)$$

For this reacting system, Eq. (1) can be expressed as

$$\xi_{ATZ} = \frac{\langle r_{ATZ}(x, t_0)\rangle_{V_T} \cdot V_T}{\langle q_W(x)\rangle_{A_W} \cdot A_W} \quad (2)$$

$$\xi_{ATZ} = \frac{\left(C_{ATZ,t_0} - C_{ATZ,t_f}\right) \cdot V_T}{(t_f - t_0) \cdot \langle q_W(x)\rangle_{A_W} \cdot A_W} \quad (3)$$

Where $\langle r_{ATZ}(x, t_0)\rangle_{V_T}$ represents the ATZ degradation rate, $(t_f - t_0)$ is the time interval of the experimental run, V_T the total volume of reaction (L), C_{ATZ,t_0} and C_{ATZ,t_f} are ATZ concentrations at initial and final time (t$_0$ and t$_f$), respectively, (mol L^{-1}), and $\langle q_W(x)\rangle_{A_W}$ represents the incident radiation flux (Einstein cm^{-2} s^{-1}) at the reactor window averaged over the window area (A$_W$) (cm^{-2}).

4. Results and discussion

4.1. Preliminary runs

Initially, different types of previous experiments were carried out in order to investigate the effects of initial catalyst concentrations (C$^0_{CAT}$), H$_2$O$_2$ to ATZ initial molar ratios (R) and radiation levels (Rad) on the catalytic activity of one of the synthesized materials, Fe/MCM-41(2.5).

The effect of initial catalyst concentration (C$^0_{CAT}$ = 0.5, 1 and 1.5 g L^{-1}) on the ATZ degradation for a constant value of R (equal to 175), is presented in Fig. 2. Additionally, the figure shows a similar study employing three different values of R: 35 (stoichiometric requirement), 175 and 350, for a constant value of C$^0_{CAT}$ (equal to 1 g L^{-1}). In both cases, radiation level was 100% i.e. all lamps lit. Finally, Fig. 2 also illustrates the experimental results of the ATZ conversion as a function of radiation levels: 0 (without radiation), 50% (only two lamps lit) and 100% (all lamps lit), for a constant value of C$^0_{CAT}$ and R.

When looking at the ATZ degradation in this figure, it should be noted that an increase of the initial catalyst concentration, from 0.5 to 1 g L^{-1}, introduces an increase on the pollutant conversion. Conversely, a significant decrease of the ATZ oxidation rate is reached
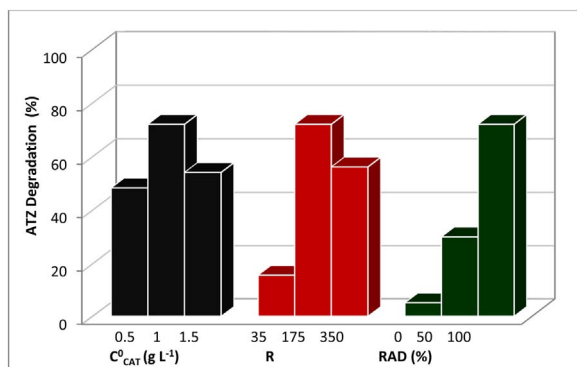
T.B. Benzaquén et al.

Fig. 2. Evolution of ATZ degradation, after 240 min for different initial catalyst concentrations of Fe/MCM-41(2.5) (R = 175 and Rad = 100%), different H_2O_2 to ATZ initial molar ratios ($C^0_{Fe/MCM-41(2,5)}$ = 1 g L^{-1} and Rad = 100%) and different radiation levels ($C^0_{Fe/MCM-41(2.5)}$ = 1 g L^{-1} and R = 175).

for C^0_{CAT} equal to 1.5 g L^{-1}. This behavior could be caused by an increase of the solid particles present in the medium, which could be overshadowing it, obstructing radiation and contributing to a notable attenuation of the activity.

Similar results are shown in the figure for different values of R, where it should be noted that for R = 35 the heterogeneous photo-Fenton degradation rates were low. However, an important increase in ATZ conversion is reached for the photo-Fenton process when R is increased from 35 to 175. In contrast, when R is increased from 175 to 350, a decrease of ATZ degradation is observed. This last run demonstrated that the oxidation rate was negatively affected by the increase of H_2O_2 concentration above the ratio R ~ 175. This is probably due to scavenging of the ·OH radicals in solution by the excess of H_2O_2, which reduces the treatment efficiency [19]. On the other hand, in the same figure, efficient pollutant degradation was achieved at the highest incident radiation. It is known that in this process the UV–vis irradiation contributes to the formation of ·OH radicals, thus the chemical oxidation is accelerated by higher irradiation levels.

From these preliminary results it is concluded that, for the heterogeneous photo-Fenton process, the optimal C^0_{CAT}, R and Rad values were 1 g L^{-1}, 175 and 100%, respectively. Therefore, the best degrading conditions of the studied pollutant could be determined and subsequently used to analyze the various synthesized catalysts.

Finally, ATZ degradation rates by homogeneous and heterogeneous photo-Fenton reactions were compared. In Fig. 3, the degradation rates of the relative ATZ concentration are presented as a function of time for homogeneous (C^0_{Fe3+} = 25 mg L^{-1}) and heterogeneous ($C^0_{Fe/MCM-}$

Table 1
Atrazine degradation and Fe leaching for each catalytic cycle.

	ATZ degradation (%)	Fe leaching (mg L^{-1})
1st cycle	65.8%	0.28
2nd cycle	66.4%	0.25
3rd cycle	64.2%	0.21

$_{41(2.5)}$ = 1 g L^{-1}, equivalent to C^0_{Fe3+} = 25 mg L^{-1}) reactions, under the same operating conditions (R = 175 and Rad = 100%). It should be noted that, previous characterization for these materials (reported in [20]) showed that the oxidation state predominant for iron was 3 +.

Comparing the homogeneous and heterogeneous photo-Fenton herbicide degradation, it can be observed that, for constant R and equivalent iron concentrations, the pollutant conversion for the homogeneous photo-Fenton reaction was higher than that obtained with the heterogeneous photo-Fenton process. Additional information about the effect of non-irradiated (Fenton) and irradiated (photo-Fenton) conditions on the homogeneous degradation processes of atrazine can be found in [21].

In addition, experimental studies of iron species leaching from Fe/MCM-41 catalyst during heterogeneous photo-Fenton degradation of ATZ were performed in order to ascertain the strength of the iron species supported on MCM-41 mesoporous matrix and the possible contribution of dissolved iron ions to the homogeneous catalytic reactions. As it is observed in Table 1, the Fe leaching values were lower than 0.3 mg L^{-1} indicating that the Fe was efficiently retained on the mesoporous surface. With these leaching values, additional runs were carried out to study the effect of the homogeneous photo-Fenton reaction at pH 5. Such values were lower than 1%, thus proving the complete heterogeneity of the catalytic reaction studied. Finally, it is important to mention that the solid synthesized here (Fe/MCM-41(2.5)) could be re-used even after three cycles without loss of activity (Table 1).

4.2. Effect of the different metal loadings into the catalyst

Using the annular photoreactor, experiments were conducted under the best previously established operating conditions for ATZ degradation. Thus, the feasibility of the ATZ degradation by the heterogeneous photo-Fenton process with different iron modified MCM-41 materials, was investigated. Fig. 4 illustrates the evolution of ATZ concentration as a function of the reaction time for different metal loadings. Five

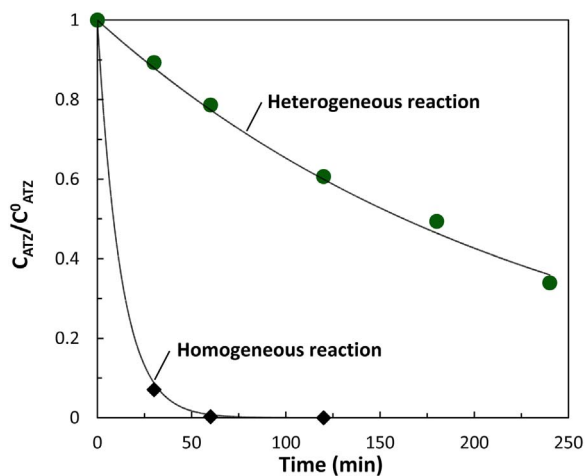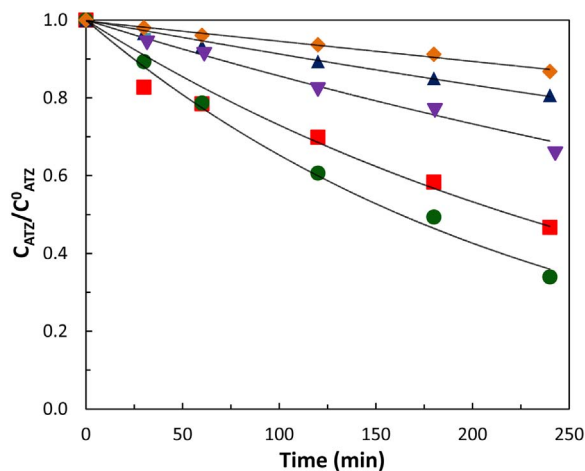**Fig. 3.** Relative ATZ concentration as a function of time, for homogeneous (♦) and heterogeneous photo-Fenton processes (●). R = 175, Rad = 100% and C^0_{Fe3+} = 25 mg L^{-1} (equivalent to $C^0_{Fe/MCM-41(2.5)}$ = 1 g L^{-1}).

Fig. 4. Relative ATZ concentration as a function of time for the heterogeneous photo-Fenton reaction, under the best experimental conditions: R = 175, C^0_{CAT} = 1 g L^{-1} and Rad = 100%. Fe/MCM-41(1) (■), Fe/MCM-41(2.5) (●), Fe/MCM-41(5) (▼), Fe/MCM-41(10) (▲) and Fe/MCM-41(15) (♦).

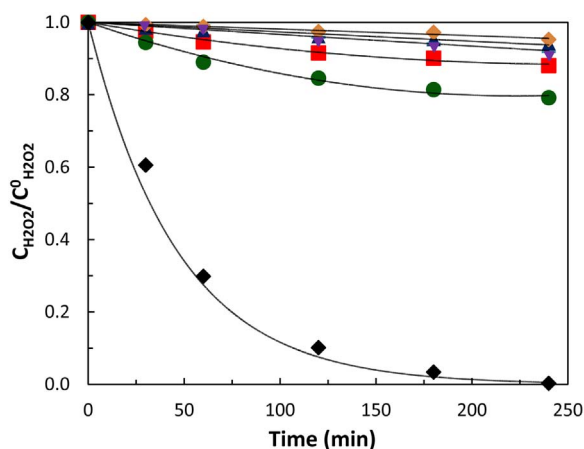**Fig. 5.** H_2O_2 relative concentration as a function of reaction time for homogeneous (♦) and heterogeneous photo-Fenton reactions. Fe/MCM-41(1) (■), Fe/MCM-41(2.5) (●), Fe/MCM-41(5) (▼), Fe/MCM-41(10) (▲) and Fe/MCM-41(15) (♦).

different values of iron loading were investigated: 1, 2.5, 5, 10 and 15 wt.%, by keeping C_{CAT}^0, R and Rad constants (using the experimental results obtained from the previous section).

As observed in this figure, when the metal loading increased from 1 to 2.5 wt.% an increase of the ATZ degradation was obtained. However, samples with higher iron contents (5, 10 and 15 wt.%) showed an important decrease in the catalytic activity. Such behavior would be giving account for the different iron species formed in the material, which will be studied in detail in the 4.4 section.

Additionally, in order to compare the behavior of the H_2O_2 concentration for the homogeneous and heterogeneous photo-Fenton processes, Fig. 5 presents the H_2O_2 concentration as a function of time for the materials developed. It is seen that, after 240 min of operation, the H_2O_2 consumption with the homogeneous reaction was 98.4% compared to 19.8% for the heterogeneous reaction with Fe/MCM-41(2.5). Consequently, the H_2O_2 consumption for all heterogeneous photo-Fenton reactions investigated was always lower than that observed with homogeneous photo-Fenton reaction.

Finally, Fig. 6 depicts the measured values of the ATZ degradation percentage and H_2O_2 consumption at 240 min as a function of the different metal loadings. It can be noted that the results obtained can be viewed as a quantitative implementation of the classical Sabatier Principle [22], which states that there is an optimum "bond strength" defining the best catalyst for a given reaction, creating a typical volcano plot. Thus, Fig. 6 shows that the ATZ degradation percentage reached a maximum of 65.3% when the Fe content was 2.5 wt.%. This shows how the activity of different catalysts varies as a function of the Fe nominal loading.
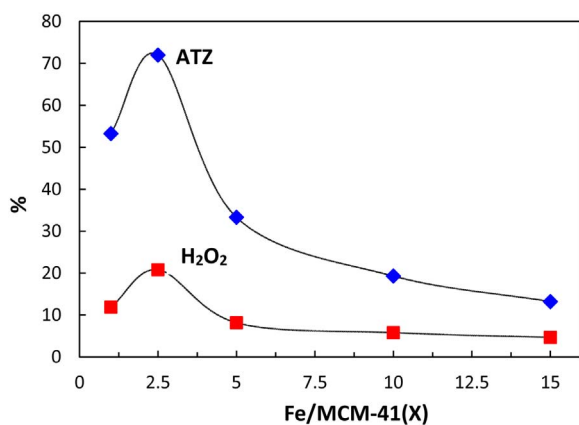

Fig. 6. Volcano plots for the ATZ degradation and H2O2 consumption after 240 min, for all samples modified with Fe, $C_{CAT}^0 = 1$ g L^{-1}. ATZ degradation (%) (♦) H2O2 consumption (%) (■).

It is interesting to highlight that, although the behavior of the H_2O_2 consumption (Fig. 6) was assimilated to the degradation behavior of contaminant, the higher loaded samples (Fe/MCM-41(5), Fe/MCM-41(10) and Fe/MCM-41(15)) exhibited constant H_2O_2 consumptions for lower pollutant conversions. This behavior could evidence a change in the iron species present in these last materials, which could decompose the H_2O_2.

4.3. Photonic efficiency

According to Eq. (2), to determine the relative photonic efficiencies is necessary to calculate the incident radiation flux at the reactor window (q_W). This value was calculated from actinometric measurements [23]. The net radiative flux (all lamps lit) at the reactor wall (783.5 cm^2) was determined to be 6.96×10^{-9} Einstein cm^{-2} s^{-1}. The same method was used to corroborate that the radiative flux at the reactor wall with only two lamps lit was approximately half (3.41×10^{-9} Einstein cm^{-2} s^{-1}).

Once the radiative fluxes for different radiation levels were calculated, the photocatalytic heterogeneous reactions with Fe/MCM-41(2.5) for ATZ oxidation were planned, according to three-level factorial designs (3^k) (one for RAD = 100% and the other for RAD = 50%), within the following experimental domain:

- Factor 1: H_2O_2 to ATZ initial molar ratios, R. *Levels:* 35, 175 and 350.
- Factor 2: Initial catalyst concentration, $C_{Fe/MCM-41(2.5)}^0$ (g L^{-1}). *Levels:* 0.5, 1 and 1.5.

Table 2 presents a summary of the operating conditions for the experimental program and values of ξ_{ATZ} calculated from Eq. (3). Fig. 7 illustrates 3D graphics of photonic efficiencies after a reaction time t = 240 min, as a function of R and $C_{Fe/MCM-41(2.5)}^0$, for different radiation levels.

Under the experimental conditions employed in this work, we have detected optimal values of R and $C_{Fe/MCM-41(2.5)}^0$ for the two radiation levels studied. As it can be observed, for both radiation levels, at R = 35 the ATZ degradation rates are low; however, an increase in ATZ conversion is reached when R is increased from 35 to 175. Conversely, for higher oxidant concentrations (R = 350), H_2O_2 acts as a radical "scavenger", competing with the pollutant degradation, reducing the ATZ conversion and consequently the photonic efficiencies. On other hand, for both experimental designs, it can be observed that the photonic efficiencies for ATZ degradation increase when C_{CAT}^0 is

Table 2
Photonic efficiency for the ATZ degradation.

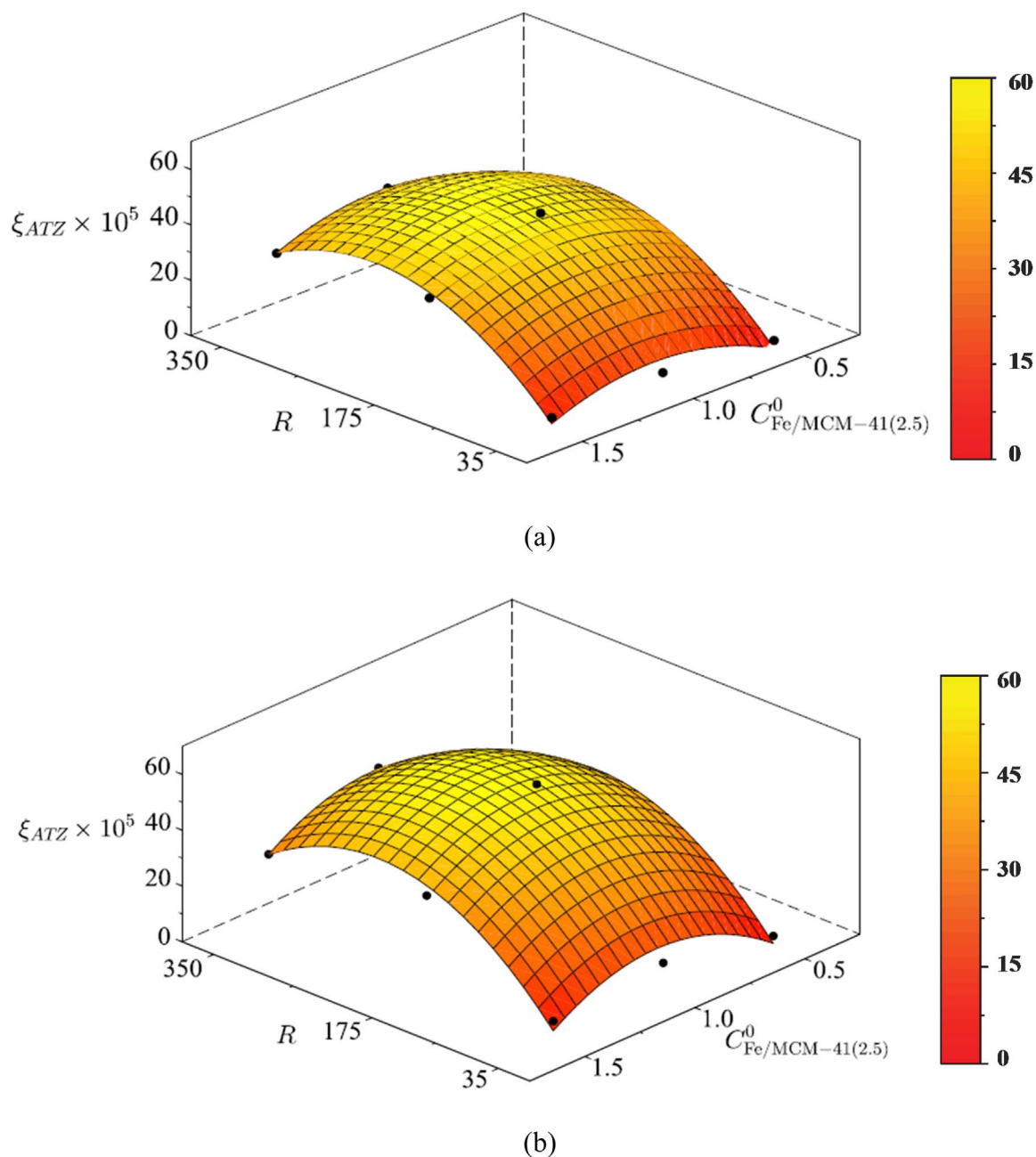| RAD (%)	R	$C_{Fe/MCM-41(2.5)}^0$ (g L^{-1})	$(C_{ATZ,t0}-C_{ATZ,tf})$ x 10^6 (mol L^{-1})	ξ_{ATZ} x 10^5 (mol Einstein^{-1})
50	35	0.5	1.0	1.3
50	35	1.0	4.0	5.2
50	35	1.5	3.4	4.4
50	175	0.5	20.0	26.1
50	175	1.0	35.4	46.0
50	175	1.5	23.7	30.9
50	350	0.5	17.7	23.0
50	350	1.0	26.3	34.2
50	350	1.5	20.1	26.1
100	35	0.5	5.7	3.6
100	35	1.0	18.1	11.5
100	35	1.5	12.8	8.1
100	175	0.5	51.8	32.9
100	175	1.0	90.1	57.3
100	175	1.5	55.0	35.0
100	350	0.5	36.5	23.2
100	350	1.0	63.8	40.6
100	350	1.5	42.8	27.1

(a)

(b)

Fig. 7. Photonic efficiencies for the ATZ degradation. Keys: a) RAD = 50% and b) RAD = 100%.

increased from 0.5 to 1 g L^{-1}. Then, above this catalyst concentration, the increase of the solid particles present in the medium could be obstructing the incident radiation and decreasing the activity.

Finally, it noteworthy that no significant increases in the photonic efficiencies were observed when RAD was changed from 50% to 100%, for R = 350. This behavior can be attributed to the fact that the increase of net radiative flux (for RAD = 100%) averaged over the reactor windows (denominator of Eq. (3)) can be comparable to the slight increase of the ATZ degradation rate (numerator of Eq. (3)).

4.4. Morphological and structural characterization of the samples

All of the materials synthesized in this study were characterized according to Cuello et al. [20]. All the samples exhibit X-ray diffraction patterns (XRD) typical of the MCM-41 mesoporous structure [13,24]. However, a reduction in the peak intensities is observed when the metal loading increases, probably due to the formation of oxide clusters or

Table 3
Structure properties and chemical composition of the Fe/MCM-41(x) synthesized.

	Area[a] (m^2 g^{-1})	V$_{TP}$ (cm^3 g^{-1})	Fe content (wt.%)[b]
MCM-41	996	0.70	–
Fe/MCM-41(1)	996	0.72	0.93
Fe/MCM-41(2.5)	948	0.71	2.55
Fe/MCM-41(5)	923	0.69	4.25
Fe/MCM-41(10)	801	0.59	8.34
Fe/MCM-41(15)	747	0.54	12.54

[a] Determined by BET.
[b] Determined by ICP method.

nanoparticles. Then, the structure properties and chemical composition for all the samples synthesized are shown in Table 3. All the samples exhibit pore sizes around 3.5 nm, high areas and pore volumes typical of MCM-41 structures. Nevertheless, a meaningful reduction in these
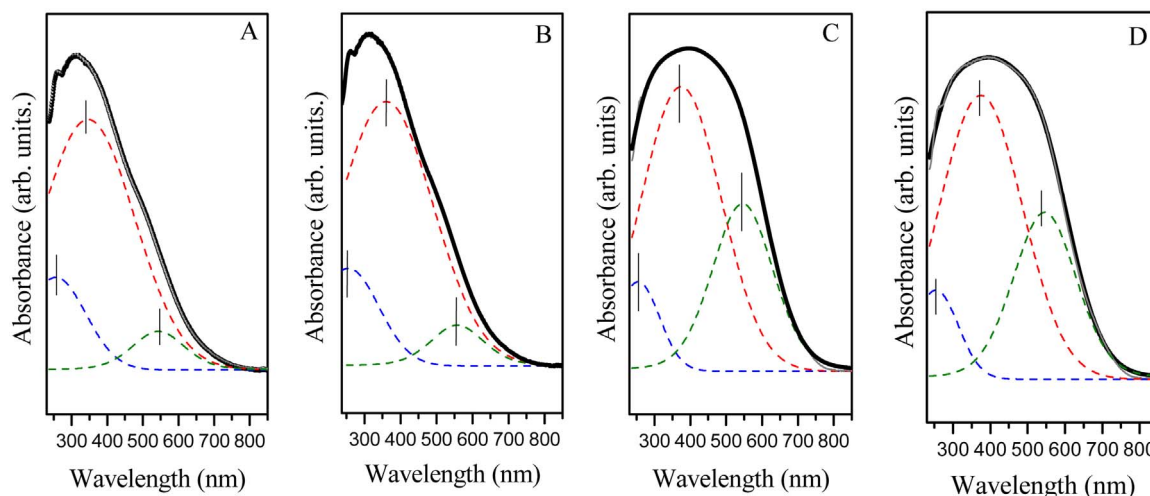
Fig. 8. UV–vis DR spectral of the MCM-41 samples synthesized with different Fe contents. Fe/MCM-41(1), Fe/MCM-41(2.5), Fe/MCM-41(5) and Fe/MCM-41(15).

values was observed for the Fe nominal loadings of 10 and 15 wt.%. Again, this behavior can be attributed to the increase in amount and size of the iron oxide species formed both inside the channels and on the external surface, which would be blocking some porous channels.

UV–vis DR spectroscopy is a useful method to characterize the coordination environment of transition metals supported on a porous network and determine the presence of metallic species on the material [24]. The UV–vis DR spectra of all the investigated samples have been deconvoluted into three bands, which can be assigned to the different Fe species. Fig. 8 shows the deconvolutions corresponding to the Fe/ MCM-41(1), Fe/MCM-41(2.5) and Fe/MCM-41(15) samples considered as representative. The first maximum at about 254 nm indicates that iron atoms are able to link to surface O atoms [25]. Then, while the second maximum at about 378 nm can be attributed to iron oxide clusters (FeO)n or nanoparticles of very small size [26], the third maximum at about 545 nm can be assigned to larger iron oxide nanoparticles [27]. As noted, the evolution of the speciation of iron depends on the loading degree. Thus, the iron can be stabilized as isolated cations on the support until certain saturation coverage is reached. Beyond this limit, a clustering process would lead to the formation of very small oligonuclear (FeO)n oxides, probably with low oxygen coordination, and finally to the iron oxide nanoparticles [24]. As it is observed in Fig. 8, the samples with high iron loadings show an increased presence of larger iron oxide nanoparticles. Such species, according to the catalytic results obtained in the previous section, could lead to a blocking of the isolated Fe^{3+} species (maximum at about 254 nm in UV–vis DR spectra) responsible for the activity of the solids. Thus, such samples present a decrease in the catalytic activity (Fig. 4).

Additionally, the results of the structural and chemical characterization could also explain the H_2O_2 concentration behavior on the experimental runs for the catalysts with Fe nominal loadings above 2.5 wt.%. As explained before, the higher loaded samples exhibited constant H_2O_2 consumptions although a considerably lower pollutant conversion was obtained (Fig. 6). This behavior could be caused by the high amount of iron oxide species found in the materials surface, which can decompose the H_2O_2 present in the medium into water and hydrogen [28]. Thus, in these cases, it is not possible to directly associate the H_2O_2 consumption with the ATZ degradation obtained.

Transmission electron microscopy (TEM) was used to extend the structural analysis presented from XRD. Fig. 9A shows the TEM image of the synthesized pure matrix which exhibit well-ordered parallel straight mesochannels, characteristic of the regular and hexagonal pore arrangement of MCM-41 type materials. Then, as it can be observed in Fig. 9B_1 and B_2 the Fe/MCM-41(2.5) sample does not show a notable loss of the structure. In addition, since the darker areas in TEM images

represent the electronically more dense phases, the existence of some very small oxide clusters, evidenced by the small black spots along the mesopores, was corroborated.

5. Conclusions

MCM-41 mesoporous silicates with different Fe contents were synthesized by the wet impregnation method, a simple and inexpensive synthesis pathway. All of the materials exhibited high specific surface, pore volume and good structural regularity retaining the MCM-41 structure after the metal incorporation.

The mesostructured iron-containing materials have been successfully tested for the heterogeneous photo-Fenton degradation of atrazine in aqueous solutions. Besides, it was demonstrated that both heterogeneous and homogeneous photo-Fenton reactions are appropriate treatments for water containing atrazine. Although the pollutant conversion for the homogeneous photo-Fenton reaction was higher than that obtained with the heterogeneous photo-Fenton process, it is important to remark that the heterogeneous reaction was carried out at near-neutral pH and with a lower consumption of hydrogen peroxide.

The effect of the different metal loadings into the catalyst over Atrazine degradation by the heterogeneous photo-Fenton process was investigated. As a result, it was shown that when the Fe content was 2.5 wt.% the pollutant degradation reached a maximum value. Then, in order to compare the effects of the most significant operating variables (initial hydrogen peroxide concentration, initial catalyst concentration and radiation level) on atrazine degradation, the photonic efficiencies were evaluated using Fe/MCM-41(2.5). Optimal values of R and $C_{Fe/MCM-41(2.5)}^0$ were detected for the two radiation levels studied. Thus, it was demonstrated that the photonic efficiencies were negatively affected by an increase of initial hydrogen peroxide concentration above R = 175 and of initial catalyst concentration above 1 g L^{-1}. In addition, the efficiency of the system is not significantly improved by an increase of the levels of UV-radiation for R = 350.

Finally, the evolution in the iron speciation on solids for different metal loadings was also investigated. Several iron species were detected and, nature, dispersion and size of such species, was correlated with the different catalytic behaviors of the nanocomposites. It was found that iron oxide nanoparticles increased in amount and size when the Fe loading was increased (5, 10 and 15 wt.%) indicating a possible blocking of isolated Fe^{+3} species responsible for the activity of the solid (active sites). Consequently, the Fe/MCM-41(2.5) appears as a very promising catalyst for a heterogeneous photo-Fenton process of pre-treatment, capable of enhancing the biodegradability of water contaminated with biorecalcitrant chemicals, as the herbicide atrazine.
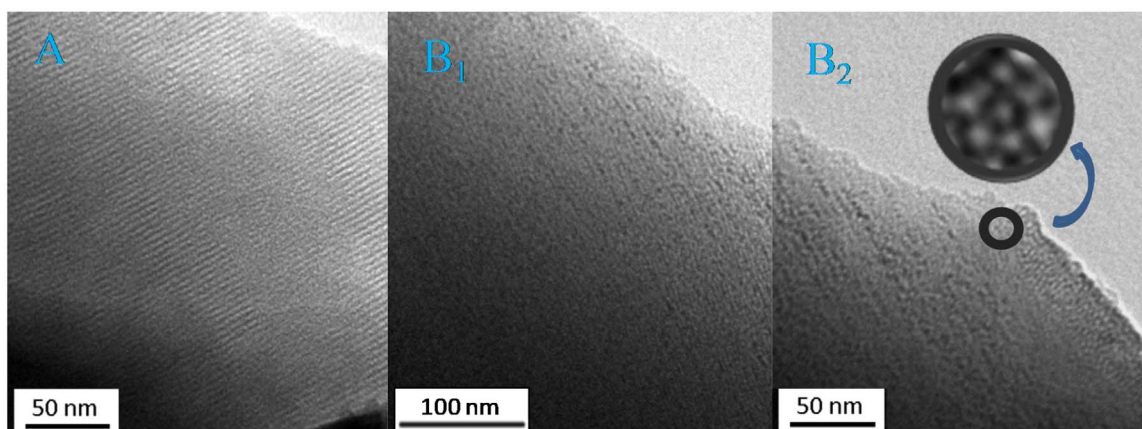
Fig. 9. TEM images of the pure MCM-41 (A) and Fe/MCM-41(2.5) sample (B).

6. Funding sources

References

[1] I. Oller, S. Malato, J.A. Sanchez-Peréz, M.I. Maldonado, R. Gassó, Catal. Today 129 (2007) 69–78.

[2] T.B. Benzaquén, M.T. Benzzo, M.A. Isla, O.M. Alfano, Water Sci. Technol. 67 (2013) 210–216.

[3] J.J. Pignatello, E. Oliveros, A. MacKay, Crit. Rev. Environ. Sci. Technol. 36 (2006) 1–84.

[4] L. Guo, F. Chen, X. Fan, W. Cai, J. Zhang, Appl. Catal. B Environ. 96 (2010) 162–168.

[5] A. Soon, B. Hameed, Desalination 269 (2011) 1–16.

[6] N. Banić, B. Abramović, J. Krstić, D. Šojić, D. Lončarević, Z. Cherkezova–Zheleva, V. Guzsvány, Appl. Catal. B: Environ. 107 (2011) 363–371.

[7] Y. Du, L. Zhao, Y. Su, J. Hazard. Mater. 195 (2011) 291–297.

[8] M.V. Phanikrishna Sharma, V. Durga Kumari, M. Subrahmanyam, Chemosphere 72 (2008) 644–651.

[9] C. Kresge, M. Leonowicz, W. Roth, J. Vartuli, J. Beck, Nature 359 (1992) 710–712.

[10] J.S. Beck, J.C. Vartuli, W.J. Roth, M.E. Leonowicz, C.T. Kresge, K.D. Schmitt, C.T.W. Chu, D.H. Olson, E.W. Sheppard, S.B. McCullen, J.B. Higgins, J.L. Schlenker, J. Am. Chem. Soc. 114 (1992) 10834–10843.

[11] N.A. Fellenz, J.F. Bengoa, S.G. Marchetti, A. Gervasini, Appl. Catal. A: Gen. 435–436 (2012) 187–196.

[12] N.I. Cuello, V.R. Elías, S. Urreta, M. Oliva, G.A. Eimer, Mater. Res. Bull. 48 (2013) 3559–3563.

[13] V.R. Elías, M.I. Oliva, S. Urreta, S.P. Silvetti, K. Sapag, A.M. Mudarra Navarro, S.G. Casuscelli, G.A. Eimer, Appl. Catal. A Gen. 381 (2010) 92–100.

[14] A.O. Allen, J.A. Hochanadel, J.A. Ghormley, T.W. Davis, J. Phys. Chem. 56 (1952) 575–586.

[15] APHA AWWA WEF Standard Methods for the examination of Water and Waste Water, 19th Ed., 1995.

[16] J. Villarroel Rocha, D. Barrera, K. Sapag, Top. Catal. 54 (2011) 121–134.

[17] S.E. Braslavsky, A.M. Braun, A.E. Cassano, Al. V. Emeline, M.I. Litter, L. Palmisano, V.N. Parmon, N. Serpone, Pure Appl. Chem. 83 (2011) 931–1014.

[18] T.B. Benzaquén, M.A. Isla, O.M. Alfano, Water Sci. Technol. 66 (2012) 2209–2216.

[19] A.C.S.C. Teixeira, R. Guardani, C.A.O. Nascimento, Ind. Eng. Chem. Res. 42 (2003) 5751–5361.

[20] N.I. Cuello, V.R. Elías, C.E. Rodriguez Torres, M.E. Crivello, M.I. Oliva, G.A. Eimer, Microporous Mesoporous Mater. 203 (2015) 106–115.

[21] T.B. Benzaquén, M.A. Isla, O.M. Alfano, J. Chem. Technol. Biotechnol. (2014) 459–467 90 pp..

[22] M. Boudart, G. Ertl, H. Kn€ozinger, J. Weitkamp, Handbook of Heterogeneous Catalysis, Wiley-VCH, Weinheim, 1997, p. 1.

[23] S.L. Murov, I. Carmichael, G.L. Hug, Handbook of Photochemistry, 2nd edition, Marcel Dekker, New York, 1993.

[24] V. Elías, E. Sabre, E. Winkler, M.L. Satuf, E. Rodriguez-Castellón, S.G. Casuscelli, G.A. Eimer, Microporous Mesoporous Mater. 163 (2012) 85–95.

[25] A. De Stefanis, S. Kaciulis, L. Pandolfi, Micropor Mesopor Mater. 99 (2007) 140–148.

[26] V.R. Elías, E.V. Sabre, E.L. Winkler, S.G. Casuscelli, G.A. Eimer, Appl. Catal. A 467 (2013) 363–370.

[27] L. Chmielarz, P. Kustrowski, R. Dziembaj, P. Cool, E. Vansant, Appl. Catal. 62 (2006) 369–380.

[28] Y. Suh, N. Kim, W. Ahn, H. Rhee, J. Mol. Catal. A: Chem. 174 (2001) 249–254.